

Impact of calcium on N1 influenza neuraminidase dynamics and binding free energy

Morgan Lawrenz,^{1,2*} Jeff Wereszczynski,¹ Rommie Amaro,^{3,4} Ross Walker,⁵ Adrian Roitberg,⁶ and J. Andrew McCammon^{1,2,7,8}

¹ Department of Chemistry and Biochemistry, University of California, San Diego, La Jolla, California

² Center for Theoretical Biological Physics, University of California, San Diego, La Jolla, California

³ Department of Pharmaceutical Sciences, University of California, Irvine, California

⁴ Department of Computer Science, University of California, Irvine, California

⁵ San Diego Supercomputer Center, University of California, San Diego, California

⁶ Quantum Theory Project, University of Florida, Gainesville, Florida

⁷ Department of Pharmacology, UCSD, La Jolla, California

⁸ Howard Hughes Medical Institute, University of California, San Diego, La Jolla, California

ABSTRACT

The highly pathogenic influenza strains H5N1 and H1N1 are currently treated with inhibitors of the viral surface protein neuraminidase (N1). Crystal structures of N1 indicate a conserved, high affinity calcium binding site located near the active site. The specific role of this calcium in the enzyme mechanism is unknown, though it has been shown to be important for enzymatic activity and thermostability. We report molecular dynamics (MD) simulations of calcium-bound and calcium-free N1 complexes with the inhibitor oseltamivir (marketed as the drug Tamiflu), independently using both the AMBER FF99SB and GROMOS96 force fields, to give structural insight into calcium stabilization of key framework residues. Y347, which demonstrates similar sampling patterns in the simulations of both force fields, is implicated as an important N1 residue that can “clamp” the ligand into a favorable binding pose. Free energy perturbation and thermodynamic integration calculations, using two different force fields, support the importance of Y347 and indicate a +3 to +5 kcal/mol change in the binding free energy of oseltamivir in the absence of calcium. With the important role of structure-based drug design for neuraminidase inhibitors and the growing literature on emerging strains and subtypes, inclusion of this calcium for active site stability is particularly crucial for computational efforts such as homology modeling, virtual screening, and free energy methods.

Proteins 2010; 78:2523–2532.
© 2010 Wiley-Liss, Inc.

Key words: oseltamivir; thermodynamic integration; Bennett Acceptance Ratio; force field comparison; metal binding; molecular dynamics.

INTRODUCTION

Type A influenza virus is becoming a worldwide pandemic threat due to its virulence and transmissibility in people.^{*} The viral surface protein neuraminidase, along with hemagglutinin, classifies influenza subtypes and fulfills an important role in viral propagation by cleaving a terminal sialic acid from host cell surfaces; thus, neuraminidase is a key drug target for controlling flu infection. The enzyme has two distinct families,¹ group 1 (N1, N4, N5 and N8) and group 2 (N2, N3, N6 and N7), with group 1 including the N1 subtype found in recent outbreaks of the highly pathogenic subtype H5N1, as well as the 1918 epidemic and “swine flu” H1N1. The protein exhibits a high rate of antigenic shift and drift, yielding proteins with heterogeneous sequences that can reduce sensitivity to the clinically used inhibitors oseltamivir (marketed as Tamiflu by Roche Pharmaceuticals, Basel, Switzerland), zanamivir (marketed as Relenza by GlaxoSmithKline, Bentford), and peramivir (BioCryst Pharmaceuticals, Birmingham, AL).

A high-affinity calcium binding site near the active site has been identified through crystallography^{1–4} and Proton Induced X-ray Emission (PIXE) experiments,⁵ though the calcium density was not resolved or discussed for some holo structures of group 1 neuraminidase.¹ The specific role of this calcium ion is unknown, but experiments have supported its importance for wild-type enzyme activity⁶ and enzyme

*<http://www.cdc.gov/flu/avian/gen-info/flu-viruses.htm>.

Additional Supporting Information may be found in the online version of this article.
Grant sponsor: Large Allocations Resource Committee; Grant number: TG-MCA05S010;
Grant sponsor: UC Lab Award; Grant number: 09-LR-06-117792; Grant sponsor: NSF Teragrid Award; Grant number: TG-MCB090110

*Correspondence to: Morgan Lawrenz, Department of Chemistry and Biochemistry, University of California, San Diego, La Jolla, California. E-mail: mlawrenz@ucsd.edu

Received 18 February 2010; Revised 9 April 2010; Accepted 19 April 2010

Published online 3 May 2010 in Wiley InterScience (www.interscience.wiley.com).

DOI: 10.1002/prot.22761

thermostability⁷. Commonly performed fluorometric neuraminidase activity assays include calcium salts in the activity buffer and follow the protocol developed originally by Potier *et al.*,⁸ where increased calcium ion concentration was found to augment activity. In addition, a recent crystal structure of calcium-deficient group 2 neuraminidase shows destabilization of the key active site residue R292 near the calcium binding site.⁹

Although dynamics of N1 ligand binding have been examined computationally,^{10–13} no dynamic, structural study has investigated the contribution of this calcium to neuraminidase substrate binding. Here, we compare simulations of calcium-bound and calcium-free complexes of N1 neuraminidase bound to the FDA-approved, nanomolar-affinity drug oseltamivir. To quantify the impact of this calcium on oseltamivir binding affinity, we calculate the free energy of binding for both complexes. This study also checks for force field dependency of the observed calcium effects on N1 dynamics through comparison of simulations and free energy calculations performed with the AMBER FF99SB and GROMOS96 force fields.

We emphasize the impact of calcium binding on integrity of the active site and accurate calculation of binding free energies. In particular, for N1, calcium stabilizes Y347 for interaction with the ligand and helps to maintain an optimal binding pose with other N1 binding site residues. Incorporation of calcium as an integral part of the active site is particularly crucial given the importance of structure-based drug design for N1 inhibitor development to date¹⁴ and prevalence of homology models^{15,16} for emerging subtypes and resistance mutations, virtual screening,^{17,18} and free-energy methods^{19–21} for this protein.

MATERIALS AND METHODS

N1 monomer simulations were performed using the GROMOS05 software for biomolecular simulation²² and the GROMOS96 force field (45A3 parameter set).²³ Molecular Dynamics (MD) set up is described in detail in the Supporting Information Methods section. Both complexes of N1-oseltamivir, with and without the bound calcium ion, were simulated in 10 independent trajectories, each 4 ns, for a total of 40 ns of simulation for each complex. Comprising the 10 simulations were five simulations generated from the chain B monomer in the oseltamivir-bound Loop 150 “open” crystal structure (PDBID: 2HU0) and five simulations started from the chain A monomer in the holo Loop 150 “closed” crystal structure (PDBID: 2HU4). As the calcium density was not present in these crystal structures, overlap with the apo N1 structure 2HTY aided in positioning of the ion in the protein; the calcium was parametrized in the classical force field. To generate the independent trajectories, these structures were each initialized with random veloc-

ities assigned from a Maxwell–Boltzmann distribution at 5 K.

Two 100 ns N1 tetramer simulations with the AMBER FF99SB force field^{24,25} were performed, each with atomic coordinates taken from the holo, open Loop 150 crystal structure (2HU0) and with the calcium inserted from overlap with the apo 2HTY structure. Calcium-bound simulations used the PMEMD module in AMBER 10,²⁶ whereas calcium-free simulations were performed using the Desmond Molecular Dynamics package developed by D.E.Shaw Research.²⁷ For details of these simulations, please see the Supporting Information Methods section. Although there are a few differences in the specifics of the MD engines used to run the AMBER FF99SB simulations (Supporting Information Methods), the similarity in RMSF (Supporting Information Fig. 1) indicates similar sampling of conformational space. AMBER FF99SB trajectories for each monomer of the tetramer were extracted and concatenated to approximate 400 ns of monomer N1 sampling.

Analysis tools in Visual Molecular Dynamics (VMD)²⁸ were applied for calculation of root mean squared fluctuation (RMSF) and deviation (RMSD), and monitoring of torsion, hydrogen bonds, and salt bridge distances. Hydrogen bond criteria applied a donor–acceptor distance cutoff of 3.5 Å and a 120° cutoff for the donor-hydrogen-acceptor angle. For analysis, structures were extracted every 10 ps for each 400 ns AMBER FF99SB trajectory and 2 ps for the 40 ns GROMOS96 trajectories. These structures were used for the GROMOS RMSD clustering algorithm,²⁹ applied using the cluster2 program in GROMOS05 software.²² A rotational and translational fitting was applied to all the C_α carbons, followed by application of the RMSD clustering to all atoms of 41 residues that comprise the binding site (residues 117–119, 133–138, 156, 178–179, 196–200, 223–228, 243–247, 276, 277, 292–295, 344–347, 371, 401, 402). This selection is similar to that used for relaxed complex docking of N1 in Cheng *et al.*,¹⁸ but here we exclude residues in the highly flexible Loop 150 (residues 147–152) and Loop 430 (430–439) regions to focus the algorithm on the active site portion near the calcium binding site. After screening a variety of RMSD cutoff values for cluster generation, using the total number and diversity of clusters as criteria, a value of 1.5 Å was selected for the GROMOS96 trajectories, and a value of 1.2 Å for AMBER FF99SB trajectories. The discrepancy in the chosen RMSD cutoff, as well as the varied cluster populations, can be attributed to the varied potential energy landscapes produced by the different force fields, as well as the use of multiple, shorter GROMOS96 trajectories and fewer, longer AMBER FF99SB simulations.

Two different, rigorous binding free energy calculations were used: free energy perturbation (FEP), with the AMBER FF99SB force field, and thermodynamic integration (TI) with the GROMOS96 force field. Both bound

and unbound calculations were performed, to give a $\Delta G_{\text{protein}}$ from decoupling the bound oseltamivir from N1, and a ΔG_{water} from decoupling of unbound oseltamivir, free in a box of water. Following the thermodynamic cycle involved in double decoupling,^{30,31} $\Delta G_{\text{protein}}$ is subtracted from ΔG_{water} to give ΔG_{bind} .

The GROMOS05²² software was used for both oseltamivir-bound and oseltamivir-unbound TI calculations, repeated in independent trajectories (IT-TI). For the bound state decoupling, six calculations decoupled oseltamivir from the ion-bound complex, and six decoupled the ligand from the ion-free complex, for a total of 12 N1 TI calculations. For each of these complexes, the calculations were performed in triplicate, with different starting structures that capture diverse conformations of Loop 150; three calculations were initialized from a closed Loop 150 N1 conformation, and three were initialized from an open Loop 150 conformation. These starting structures were extracted from the independent MD trajectories described above, after 1 ns of equilibration. Six independent oseltamivir-unbound TI calculations decoupled oseltamivir from a $37 \times 37 \times 37 \text{ \AA}^3$ box of SPC water. For each TI, 26 windows span the λ range from 0.00 (ligand coupled) to 1.00 (ligand decoupled), in 0.04 intervals. For ligand–protein decoupling, a 500 ps equilibration period preceded a 500 ps sampling period, from which $\frac{\delta U}{\delta \lambda}$ data was recorded; the unbound decoupling calculations involved 400 ps for both equilibration and sampling periods per λ window.

To maintain a defined bound state in the protein calculations, a 0.6 kcal/mol/ \AA^2 harmonic restraint constant was applied to the C4 atom of oseltamivir and the associated volume correction³¹ + $RT\ln(CV)$ for the free energy was calculated to be −5.5 kcal/mol. Soft-core interaction potentials³² ($s_{LJ} = 0.5$ and $s_C = 0.5$) were used for ligand atoms involved in the perturbation to avoid end point singularities and to enhance sampling. For each λ window, the statistical inefficiency of the raw $\frac{\delta U}{\delta \lambda}$ data was calculated using the method described and coded by Chodera *et al.*³³ The decorrelated data was averaged to approximate $\langle \frac{\delta U}{\delta \lambda} \rangle$, which was integrated by the trapezoidal rule over the 26 λ windows for each of $N = 6$ independent calculations, as:

$$\Delta \bar{G} = \frac{\sum_{i=1}^N \int_{\lambda_0}^{\lambda_1} \delta \lambda \langle \frac{\delta U}{\delta \lambda} \rangle_\lambda}{N} \quad (1)$$

Subtraction of the $\Delta \bar{G}_{\text{protein}}$ from $\Delta \bar{G}_{\text{water}}$ gives a $\Delta \bar{G}_{\text{bind}}$. A standard error $\frac{\sigma}{\sqrt{N}}$ was computed for both $\Delta \bar{G}_{\text{protein}}$ and $\Delta \bar{G}_{\text{water}}$ over the $N = 6$ independent runs and propagated for $\Delta \bar{G}_{\text{bind}}$ (listed in Table III).

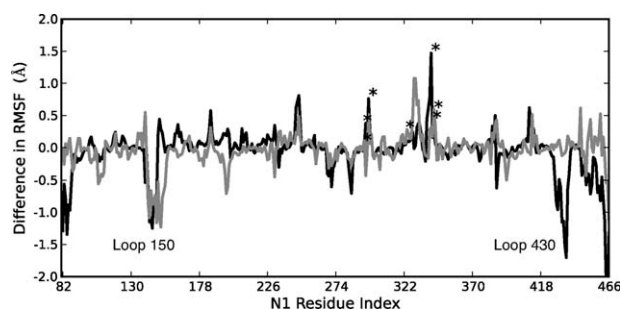
To examine the advantage of shorter, independent trajectories over a single, long trajectory in the TI calculations, one run for each set of protein TI calculations was selected for the extension of equilibration and sampling

times (1 ns equilibration and 3.8 ns sampling per λ), for an 85.8 ns increase in total sampling time for the calculation. The single $\Delta G_{\text{protein}}$ produced from each extended run differed from that of the “short” calculation result by <4%; however, the associated ΔG_{bind} was +3.3 kcal/mol less favorable than the experimentally derived target value. This discrepancy is larger than that for the IT-TI result for $\Delta \bar{G}_{\text{bind}}$, which is off the target value by +1.3 kcal/mol (Table III). The extended ion-free result was also significantly more unfavorable than the IT-TI value. This indicates that these single, extended simulations were unable to overcome sampling barriers to generate a complete ensemble average $\langle \frac{\delta U}{\delta \lambda} \rangle$. Combining multiple TI calculations initialized from diverse conformations improves sampling and can result in a more correct ΔG_{bind} .^{12,34,35}

Free energy calculations on the tetrameric complex were performed with the AMBER FF99SB force field in Desmond using FEP. For both the decoupling of unbound oseltamivir (to calculate ΔG_{water}) and bound oseltamivir (for $\Delta G_{\text{protein}}$), 21 windows were used, one with full non-bonded interaction, 10 for the annihilation of columbic interactions (with full van der Waals interactions), and 10 with the removal of van der Waals interactions (with no electrostatics). A softcore potential was used with $\alpha = 0.5$. Decoupling of unbound oseltamivir in water was performed on a system of the ligand in a $24 \times 28 \times 29 \text{ \AA}^3$ TIP3P water box with 250 ps of equilibration followed by 1 ns of sampling in each window. Bound oseltamivir decoupling calculations were performed on the tetrameric complex (from 2HU0, described above) with all four ligand molecules simultaneously removed to enhance sampling. Following 5 ns of equilibration of the starting structure, each λ window was individually equilibrated for 1 ns and then sampled for 2 ns.

Three sets of protein–ligand calculations were performed, two with the protein coordinates from the 2HU0 crystal structure (one with the bound calcium and one without) and another without calcium and initiated from clustering results in which Y347 is flipped out of the pocket (see below). Reported work functions were post-processed with the Multistate Bennett Acceptance Ratio (MBAR).³⁶ Energies were decorrelated based on their statistical inefficiencies, as in the GROMOS96 TI simulations, and error bars representing the analytic errors developed in the MBAR implementation, here represented by σ , were calculated with code made publicly available by Shirts and Chodera.[†] The free energy of decoupling the four ligands from the N1 tetramer was divided by four to obtain an average binding free energy to the N1 monomer, with a standard error $\frac{\sigma}{\sqrt{N}}$ calculated using $N = 4$.

[†]<http://simtk.org/home/pymbar>

**Figure 1**

$\text{C}\alpha$ RMSF differences for ion-free and ion-bound simulations. GROMOS96 (gray) and AMBER FF99SB (black) ion-bound RMSF is subtracted from the ion-free simulation RMSF. Asterisks indicate residues that contact the calcium ion in the 2HU0 structure.

RESULTS AND DISCUSSION

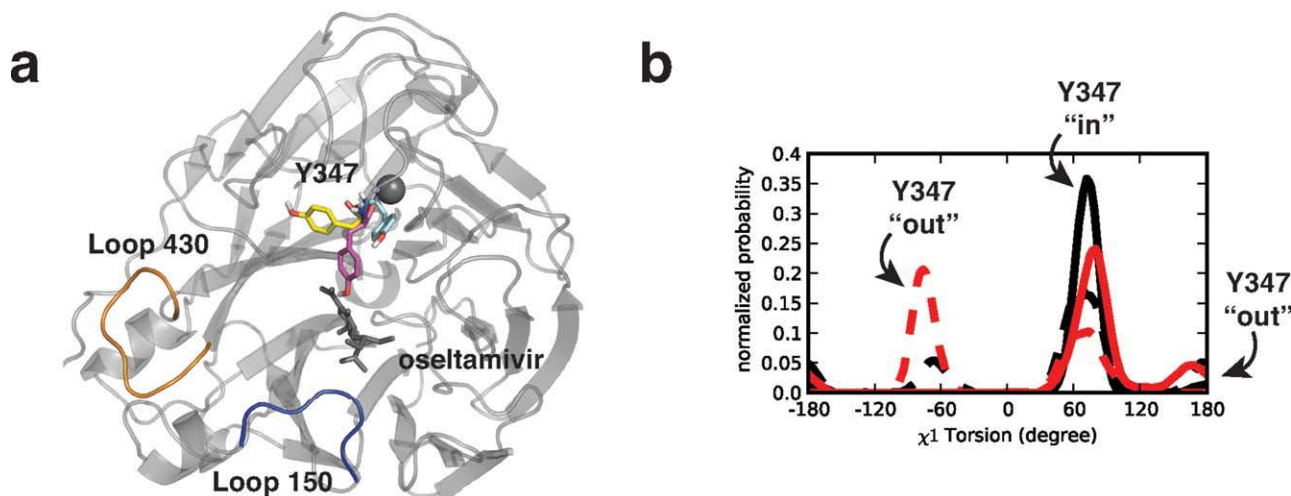
RMSF

The structure of the N1 calcium binding site includes close ion contacts with the backbone carbonyls of D293, N294, G297, G345, A346, Y347, and the carboxyl groups of both D293 and D324, with similar interactions observed in group 1 and 2 crystal structures.^{1–4,9} Therefore, removal of the ion can be expected to destabilize these residues and the loops on which they are located, leading to increased fluctuation. Both GROMOS96 and AMBER FF99SB ion-bound MD simulations were checked for similar RMSF per residue $\text{C}\alpha$ (Supporting Information Fig. 1), with the most flexibility observed for

Loop 150, Loop 430, and portions of a long disordered loop (residues 327–348) surrounding the calcium binding site. Plots of the difference in ion-free and ion-bound simulation RMSF (Fig. 1) reveal changes in backbone RMSF for these regions. Both AMBER FF99SB and GROMOS96 simulations indicate increased fluctuation near the calcium-contacting residues (see peaks near asterisks in Fig. 1), with some of the peaks corresponding to residues very close to the active site. RMSF changes are color-mapped onto the N1 monomer structure in Supporting Information Figure 2, for an overall view of where these changes occur in the protein. Loop 150 and 430 (labeled in Fig. 1) have changes in flexibility that are inconsistent in comparison of the GROMOS96 and AMBER FF99SB simulations.

Y347 torsion

Of all residues with increased mobility in the N1 ion-free simulations, Y347 has the most direct impact on ligand binding. The Y347 backbone carbonyl coordinates calcium in the N1 crystal structures^{1,4} [pink conformation in Fig. 2(a)], stabilizing the residue for interaction with the conserved ligand carboxyl group. In Figure 2(b), distributions for the tyrosine χ_1 torsion indicate a change of Y347 conformation in the ion-free simulations (dashed vs. solid lines). Torsions within the range 30–105° designate conformations that direct the sidechain into the active site for hydrogen bonding to the ligand (“in” conformation), whereas other torsion ranges correspond to conformations flipped out of the pocket and inaccessible to the ligand (“out” conformation). With the

**Figure 2**

Y347 Sampling in the N1 Active Site. (a) The N1 monomer in complex with oseltamivir (gray) and with bound calcium (gray), as well as the Y347 “in” conformation (pink) and two representative “out” conformations (yellow and cyan). (b) Normalized probability distributions for the Y347 χ_1 sidechain torsion plotted for ion-bound AMBER FF99SB (black, solid lines) and GROMOS96 (red, solid lines) simulations, compared to the corresponding distributions for ion-free simulations (dashed lines).

Table I

Change in % Occurrence of N1-Oseltamivir Hydrogen Bonds in Ion-Free Simulations Relative to Ion-Bound Simulations

Ligand moiety	Carboxyl				Ammonium			Acetamide	
	R118	R292	R371	Y347	E119	E227	E277	E227	E277
AMBER FF99SB GROMOS96	+6 -8	-13 -40	-13 -21	-14 -27	-30 -18	None ^a -49	None -35	None -16	None -3

^aIndicates no hydrogen bond observed to meet criteria described in Methods.

loss of its stabilizing backbone contact with calcium, Y347 increases sampling of “out” conformations [see cyan and yellow conformations in Fig. 2(a)].

Integration of the curves in Figure 2(b) allows for the estimation of the total time spent in the “out” Y347 conformations, whereas tracking the torsion time series indicates how often transitions occur (Supporting Information Fig. 3). In the ion-free simulations, the destabilized Y347 flips out of the pocket for 54% of the GROMOS96 simulation, and for 29% of the AMBER FF99SB simulation. Examination of each 100-ns monomer AMBER FF99SB trajectory reveals an initial “flip” after 5 ns in the chain B simulation, but no flip is seen before 13, 28, and 58 ns for chains A, C, and D, respectively (see Supporting Information Fig. 3). Five of the 10, 4 ns GROMOS96 ion-free simulations were initialized in a Y347 “out” conformation, four of which do not visit the “in” conformation. Those initialized with the “in” Y347 conformation flipped within 1.4 ns, whereas one run remained unflipped throughout 4 ns (Supporting Information Fig. 3). Thus, although the varied AMBER FF99SB and GROMOS96 simulation lengths prohibit a direct comparison of duration for the Y347 flipped conformation, the GROMOS96 simulations seem to allow more facile Y347 flipping than do the AMBER FF99SB simulations.

The “in” ligand-accessible conformation is dominant in the ion-bound simulations, with the “out” conformation occurring for only 20% and 4% of the GROMOS96 and AMBER FF99SB simulations, respectively. We note that not all conformations in the “in” torsion range result in hydrogen bond formation, but the Y347 phenol is directed toward the ligand carboxyl for potential interaction.

Hydrogen bonds

The increased sampling of Y347 “out” conformations in the ion-free simulations reduces the availability of this residue for hydrogen bonding to oseltamivir. Hydrogen bond analysis using geometric criteria (see Methods) reveals an overall reduction in the occurrence of hydrogen bonds formed between the protein and ligand for the ion-free simulations (Table I). Y347 hydrogen bond occurrence is reduced by 27% in the GROMOS96 ion-free simulations and by 14% in the AMBER FF99SB ion-free simulations.

Calcium removal affects the stability of other key binding site residues as well, resulting in reduced occurrence of hydrogen bonds to the ligand. The arginine triad, an important neuraminidase binding motif that includes R118, R292, and R371, interacts with the carboxyl of ligands.¹ A large loss of ligand hydrogen bonds to R292 and R371 is observed in the ion-free GROMOS96 simulations, and less severe but significant reductions are also observed for these residues in the AMBER FF99SB ion-free simulations. In the AMBER FF99SB simulations of both complexes, R118 only weakly meets hydrogen bonding criteria for the ligand.

With further comparison of changes in hydrogen bond occurrence, a difference in sampling becomes evident for the simulations with two different force fields. A significant reduction in hydrogen bond occurrence between the oseltamivir ammonium and the E119 carboxyl group is observed for both force fields, but the GROMOS96 simulations favor interactions of the ligand ammonium with E227 and E277; in the AMBER FF99SB simulations this ligand moiety is consistently oriented toward E119. Hydrogen bonds to residues on the flexible Loop 150 are also sampled differently in the AMBER FF99SB and GROMOS96 simulations (Supporting Information Table I). This inconsistency is also seen in the RMSF changes in Figure 1, and could be due to the different MD protocols used for GROMOS96 and AMBER FF99SB simulations, as each monomer of the AMBER FF99SB simulation was initialized in the same open Loop 150 conformation, but allowed to run for much longer periods compared to the GROMOS96 simulations (see Methods). In the AMBER FF99SB ion-free simulation, ligand hydrogen bonds to Loop 150 residues D151 and R152 are significantly reduced (Supporting Information Table I) and Loop 150 is observed to sample primarily open states (Supporting Information Fig. 4).

The protein-ligand interactions described in Table I are also largely electrostatic; monitoring changes in the distance between the center of mass for these reacting moieties [Supporting Information Fig. 5(a–d)] confirm the breaking of salt bridges and corroborate the hydrogen bonding data.

Clustering and structural changes

RMSD clustering reduces the simulation structural data to a set of representative conformations for analysis.

Table II
Summary of Cluster Populations

Cluster ^a	GROMOS96				AMBER FF99SB			
	Ion		No Ion		Ion		No Ion	
	% Ensemble	Y347	% Ensemble	Y347	% Ensemble	Y347	% Ensemble	Y347
1	24	in	39	out	93	in	50	in
2	12	in	11	in			18	out
3	9	in	10	in			15	out
4	8	out	9	out			13	out
5	8	in	9	in				
6	8	in	9	out				
7	8	out	8	out				
8	7	out						

^aClusters listed combine to represent at least 85% of the total ensemble of configurations from the simulation.

Clusters that together capture at least 85% of the total simulation ensemble are listed in Table II, with the conformation of Y347 indicated. The varied cluster populations in Table II also highlight differences in the AMBER FF99SB and GROMOS96 simulations. The cutoffs were chosen to balance resolution of unique clusters with reduction of the simulation data to a manageable number of representative conformations. The higher selected cutoff for the GROMOS96 simulations as well as the increased total number of clusters show that both GROMOS96 simulations allow more fluctuations and increased heterogeneity in sampling of conformational space; this was also indicated by higher dimensionality for GROMOS96 essential dynamics found in a broad force field comparison study.³⁷ The difference in sampling could also be attributed to the fact that the GROMOS96 simulations, which consist of ten 4 ns trajectories, may benefit from increased sampling due to the use of multiple, shorter trajectories,^{38,39} as opposed to the AMBER FF99SB simulations, which consist of fewer (four), longer (100 ns) trajectories.

Structural differences observed by comparison of cluster central members for the different force fields largely correspond to sampling differences observed in hydrogen bonding data (Table I) and RMSF changes (Fig. 1). However, both AMBER FF99SB and GROMOS96 ion-free clusters indicate changes in position of Y347 and N294, which both have backbone carbonyls directed toward the calcium and have sidechains that extend into the active site [Fig. 3(a,c)]. Other common differences occur on a solvent exposed loop near the rim of the binding site, in the 247–249 region (Fig. 1 and Supporting Information Fig. 2). Figure 3 has examples of conformational changes represented in the ion-free GROMOS96 and AMBER FF99SB clusters, which could be most pertinent for accuracy of docking or other computational free energy methods.

Destabilization of N294 due to its lost backbone contact to the calcium enables the N294 polar sidechain to

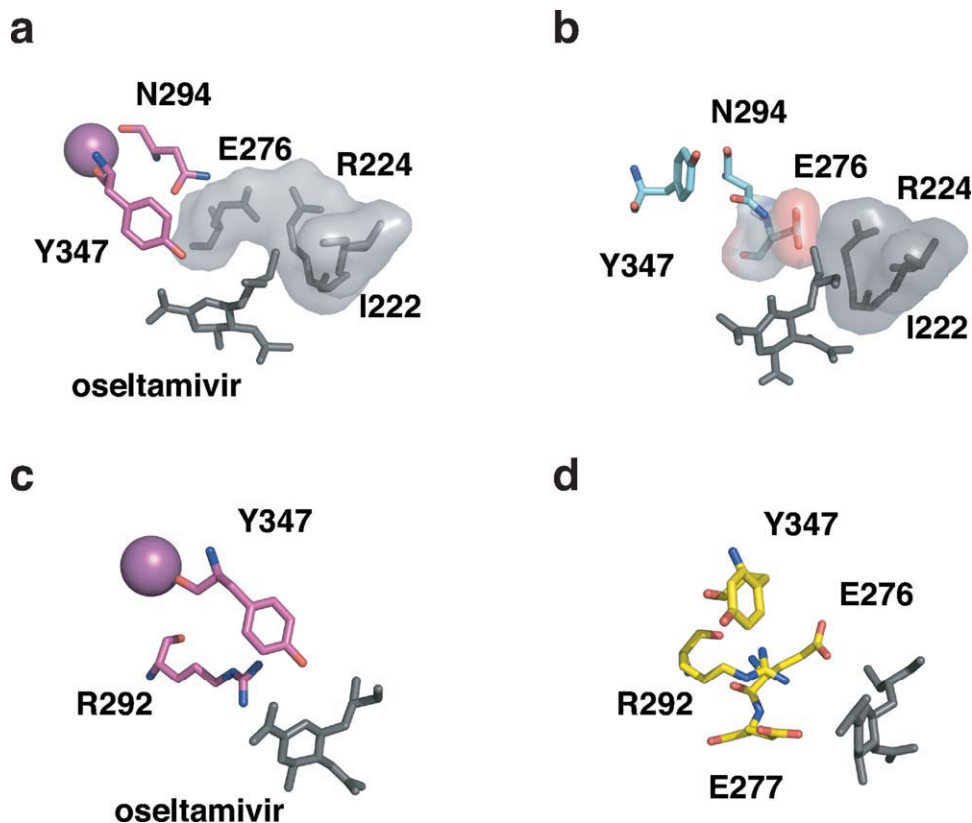
shift closer into the hydrophobic subpocket⁴⁰ that accepts the oseltamivir aliphatic tail [Fig. 3(a,b)]. This shift is further revealed by tracking the proximity of the N294 sidechain to the oseltamivir aliphatic tail throughout all simulations [Supporting Information Fig. 5(e,f)]. Instability of this residue, as well as Y347, has been proposed as the source of resistance to oseltamivir conferred by the N294S mutation in N1.⁴ In the GROMOS96 simulations, changes in R292 and E276 conformations also bring these highly polar residues closer to the hydrophobic tail of oseltamivir [Supporting Information Fig. 5(e)].

Another significant conformational change is observed in cluster four for the GROMOS96 ion-free simulation. Here, Y347 is flipped out of the pocket, and the nearby residue R292 retreats away from its electrostatic interaction with the oseltamivir carboxyl to interact with flanking glutamates E276 and E277 [Fig. 3(c,d)]. This perturbed R292 conformation is also observed in a calcium deficient crystal structure of N9 neuraminidase.⁹ In the AMBER FF99SB ion-free simulations, interaction with oseltamivir and R292 is weakened (Table I), but this conformational change is not observed.

Binding free energies

To quantify the impact of the aforementioned changes in dynamics of the N1-oseltamivir complex in absence of calcium, parallel free energy calculations were performed: free energy perturbation (FEP) with the AMBER FF99SB force field, post-processed with the MBAR method, and IT-TI with the GROMOS96 force field.

For comparison to the ion-bound FEP results (Table III) and to investigate the contribution of Y347 to the binding free energy, two sets of free energy calculations for the ion-free tetramer were carried out. The first calculation was initialized from a calcium-free structure selected after 5 ns of equilibration. During this equilibration period, Y347 had not yet flipped out of the pocket for three of the four monomers (see Supporting Informa-

**Figure 3**

Binding pose comparison for ion-bound and ion-free simulations. Oseltamivir is shown in dark gray for all panels, with residues from the top cluster of the GROMOS96 ion-bound simulation (pink) in panels (a) and (c), from the cluster four of the GROMOS96 ion-free simulation (yellow) in panel (b), and from the cluster two of the AMBER FF99SB ion-free simulation (cyan) in panel (d). The disturbed hydrophobic subpocket structure is shown with surface representation in (b) and the retreated R292 conformation in (d).

tion Fig. 2) and monitoring of the torsion throughout this calculation indicated 17% occurrence of the “out” Y347 state, compared to 6% in the calcium-bound simulation (black solid vs. black dashed in Fig. 4). Here, the free energy difference for the ion-bound and ion-free complexes is very small (Table III), which suggests that the AMBER FF99SB force field confers stability to other binding site residues and preserves an effective binding pose with oseltamivir. However, when cluster two (Table II) of the AMBER FF99SB ion-free MD simulations was selected as starting structure for each monomer in a second tetramer calculation, simulation time spent in the Y347 “out” conformation increased to 76% (green dashed line, Fig. 4). This increased destabilization of the active site framework gives more impact on the free energy of binding, with a +2.7 kcal/mol reduced favorability in $\Delta\Delta G_{\text{bind}}$. The change in results underscores both the influence of starting structure on sampling in free energy calculations, as well as the difficulty in achieving complete sampling using traditional MD methods.

The TI results are an average of six monomer calculations, initiated by structures that capture diverse confor-

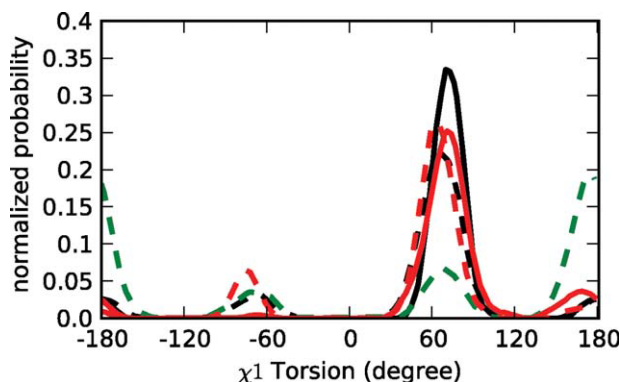
mations of Loop 150, as well as varied conformations of Y347. For the ion-free complexes, three of the starting structures include a Y347 “out” conformation, and the population of this conformation increases from 13% to 20% in the ion-free calculations (Fig. 4). This population shift is not as significant as seen for the GROMOS96 MD (Fig. 2), due to the shorter timescale of the sampling in each TI λ window and fewer independent trajectories (6 for IT-TI, 10 for the MD). Still, the calcium-free

Table III
Binding Free Energies (kcal/mol)

	Ion-bond		Ion-free	
	ΔG_{bind}	$\frac{\sigma}{\sqrt{N}}$	ΔG_{bind}	$\frac{\sigma}{\sqrt{N}}$
AMBER FF99SB with Y347 in	-14.5	1.5	-14.3	0.7
AMBER FF99SB with Y347 out			-118	1.3
GROMOS96	-15.0	2.1	-10.4	1.2
Experiment ^b	-13.7	0.2	n/a	

^a $N = 4$ for AMBER calculations and $N = 6$ for GROMOS calculations (see Methods).

^bDerived from K_i value by Kati *et al.*⁴¹

**Figure 4**

Y347 torsion changes during free energy calculations for the AMBER FF99SB ion-bound calculation (black, solid lines), AMBER FF99SB ion-free calculation with Y347 “in” starting structure (black, dashed), and with Y347 “out” starting structure (green, dashed); Also, GROMOS96 ion-bound simulations (red, solid lines) and GROMOS96 ion-free simulations (red, dashed).

$\Delta\bar{G}_{\text{bind}}$ is +4.6 kcal/mol less favorable than the ion-bound free energy value (Table III). Structural evidence for the larger impact of the calcium presence on the GROMOS96 free energy compared to the AMBER FF99SB results can be found in the more pronounced disruptions of the active site framework, a more significantly perturbed binding pose, and overall more flexibility observed in the GROMOS96 MD. However, the discrepancy between the results for the two force fields is within the reported, propagated error.

The free energy results, listed in Table III, are a close match to each other and reflect a very high, nanomolar binding affinity. From a survey of neuraminidase activity assays in the literature^{42–53} the average IC₅₀ value for oseltamivir binding to N1 is ~0.2 nM. In Table III, we compare the calculated results with a free energy value derived from the N1-oseltamivir K_i in a kinetic study by Kati *et al.*⁴¹ Both free energy results are close to this value, within the reported error. Because all binding assays in the literature include calcium salts in the activity buffer, we lack a direct experimental comparison for the ion-free results, but the reduced favorability, seen in the GROMOS free energy results and the AMBER results for predominantly “out” Y347 conformations (Table III), corresponds to an increase in K_i by ~2 orders of magnitude (from $\Delta G_{\text{bind}} = +RT \ln K_i$).

The free energy calculations, considered with the structural changes observed in the MD simulations, implicate calcium as an important factor in maintaining an effective N1 active site framework, and, in particular, through stabilization of Y347. The “in” conformation of this residue seems to “clamp” the ligand into a favorable binding pose, which includes consistent interactions with R292 and the rest of the R triad, as well as orientation of osel-

tamivir such that its branched aliphatic chain is directed to a nearby hydrophobic subpocket. The sensitivity of neuraminidase binding affinity to changes in this region of the active site is also evidenced by the oseltamivir-resistant mutations of structurally neighboring residues: R292K (N2), N294S (N1), and H274Y (N1).⁴ Y347 has been suggested¹ to prevent oseltamivir resistance to the R292K mutation in most N1 strains by providing extra stability to the binding pose, as is observed in our simulations and supported by free energy calculations. However, Y347 is mutated to an asparagine in the N1 protein of both the 1918 epidemic influenza strain and one of examined 2009 “swine flu” strains,¹⁶ which could allow susceptibility for resistance mutations.

CONCLUSION

Consistent structural changes observed in simulations with two different force fields give reinforced evidence for the structural role of calcium in stabilization of the N1 active site. Free energy results calculated using different methods and force fields agree closely with each other and with experiments to indicate a contribution of 3–5 kcal/mol to the binding free energy, or two orders of magnitude in K_i . The methods in this study also used multiple, independent simulations, initiated from diverse starting structures, in an effort to enhance sampling of the MD and obtain more accurate and reliable free energy results. Even on timescales as short as 1 ns (GROMOS96 TI), absence of the calcium causes disruption of the active site, particularly in the flipping “out” of Y347, and perturbation of the ligand binding pose. Integrity of the active site is essential for structural analysis and modeling of the N1-drug interface, often used in rational drug design. We emphasize the importance of the calcium for maintenance of this integrity and urge that it should not be excluded in N1 active site studies, particularly for structures used in docking and other computational methods. For the challenges of emerging resistance mutations in N1, which have so far occurred in the region of the active site near the bound calcium, noting the importance of framework residues in this area could also guide design of new, robust inhibitors.

ACKNOWLEDGMENTS

The authors thank the members of the McCammon group for useful discussions, particularly, Riccardo Baron for help in GROMOS simulation set up. This work used computing resources at Center for Theoretical Biological Physics (CTBP) at UCSD, Texas Advanced Computing Center (TACC), and NICS Kraken machines. Support for the McCammon group has been provided by NSF, NIH, HHMI, and NBCR.

REFERENCES

1. Russell RJ, Haire LF, Stevens DJ, Collins PJ, Lin YP, Blackburn GM, Hay AJ, Gamblin SJ, Skehel JJ. The structure of H5N1 avian influenza neuraminidase suggests new opportunities for drug design. *Nature* 2006;443:45–49.
2. Varghese JN, Laver WG, Colman PM. Structure of the influenza virus glycoprotein antigen neuraminidase at 2.9 Å resolution. *Nature* 1983;303:35–40.
3. Xu X, Zhu X, Dwek RA, Stevens J, Wilson IA. Structural characterization of the 1918 influenza virus H1N1 neuraminidase. *J Virol* 2008;82:10493–10501.
4. Collins PJ, Haire LF, Lin YP, Liu J, Russell RJ, Walker PA, Skehel JJ, Martin SR, Hay AJ, Gamblin SJ. Crystal structures of oseltamivir-resistant influenza virus neuraminidase mutants. *Nature* 2008;453:1258–1261.
5. Taylor G, Garman E, Webster R, Saito T, Laver G. Crystallization and preliminary X-ray studies of influenza A virus neuraminidase of subtypes N5, N6, N8 and N9. *J Mol Biol* 1993;230:345–348.
6. Chong AK, Pegg MS, von Itzstein M. Influenza virus sialidase: effect of calcium on steady-state kinetic parameters. *Biochim Biophys Acta* 1991;1077:65–71.
7. Burmeister WP, Cusack S, Ruigrok RW. Calcium is needed for the thermostability of influenza B virus neuraminidase. *J Gen Virol* 1994;75 (Part 2), 381–388.
8. Potier M, Mameli L, Bélisle M, Dallaire L, Melançon SB. Fluorometric assay of neuraminidase with a sodium (4-methylumbelliferyl-alpha-D-N-acetylneuraminate) substrate. *Anal Biochem* 1979;94:287–296.
9. Smith BJ, Huyton T, Joosten RP, McKimm-Breschkin JL, Zhang JG, Luo CS, Lou MZ, Labrou NE, Garrett TPJ. Structure of a calcium-deficient form of influenza virus neuraminidase: implications for substrate binding. *Acta Crystallogr D Biol Crystallogr* 2006;62:947–952.
10. Amaro RE, Minh DDL, Cheng LS, Lindstrom WM, Olson AJ, Lin J-H, Li WW, McCammon JA. Remarkable loop flexibility in avian influenza N1 and its implications for antiviral drug design. *J Am Chem Soc* 2007;129:7764–7765.
11. Amaro RE, Cheng X, Ivanov I, Xu D, McCammon JA. Characterizing loop dynamics and ligand recognition in human- and avian-type influenza neuraminidases via generalized born molecular dynamics and end-point free energy calculations. *J Am Chem Soc* 2009;131:4702–4709.
12. Lawrence M, Baron R, McCammon J. Independent-trajectories thermodynamic-integration free-energy changes for biomolecular systems: Determinants of H5N1 avian influenza virus neuraminidase inhibition by peramivir. *J Chem Theory Comput* 2009;5:1106–1116.
13. Aruksakunwong O, Malaisree M, Decha P, Sompornpisut P, Parasuk V, Pianwanit S, Hannongbua S. On the Lower Susceptibility of Oseltamivir to Influenza Neuraminidase Subtype N1 than those in N2 and N9. *Biophys J* 2007;92:798–807.
14. von Itzstein M. The war against influenza: discovery and development of sialidase inhibitors. *Nat Rev Drug Discov* 2007;6:967–974.
15. Du Q-S, Wang S-Q, Huang R-B, Chou K-C. *Chemi Phys Lett* 2010;485:191–195.
16. Wang S, Du Q, Huang R, Zhang D, Chou K. Insights from investigating the interaction of oseltamivir (Tamiflu) with neuraminidase of the 2009 H1N1 swine flu virus. *Biochem Biophys Res Commun* 2009;432–436.
17. An J, Lee DCW, Law AHY, Yang CLH, Poon LLM, Lau ASY, Jones SJM. A novel small-molecule inhibitor of the avian influenza H5N1 virus determined through computational screening against the neuraminidase. *J Med Chem* 2009;52:2667–2672.
18. Cheng LS, Amaro RE, Xu D, Li WW, Arzberger PW, McCammon JA. Ensemble-based virtual screening reveals potential novel antiviral compounds for avian influenza neuraminidase. *J Med Chem* 2008;51:3878–3894.
19. Wang NX, Zheng JJ. Computational studies of H5N1 influenza virus resistance to oseltamivir. *Protein Sci* 2009;432–436.
20. Masukawa KM, Kollman PA, Kuntz ID. Investigation of neuraminidase-substrate recognition using molecular dynamics and free energy calculations. *J Med Chem* 2003;46:5628–5637.
21. Malaisree M, Rungrotmongkol T, Decha P, Intharathep P, Aruksakunwong O, Hannongbua S. Understanding of known drug-target interactions in the catalytic pocket of neuraminidase subtype N1. *Proteins* 2008;1908–1918.
22. Christen M, Hünenberger PH, Bakowies D, Baron R, Bürgi R, Geerke DP, Heinz TN, Kastenholz MA, Kräutler V, Oostenbrink C, Peter C, Trzesniak D, van Gunsteren WF. The GROMOS software for biomolecular simulation: GROMOS05. *J Comput Chem* 2005;26:1719–1751.
23. Schuler LD, Daura X, van Gunsteren WF. An improved GROMOS96 force field for aliphatic hydrocarbons in the condensed phase. *J Comput Chem* 2001;22:1205–1218.
24. Wang J, Cieplak P, Kollman PA. *J Comput Chem* 2000;21:1049–1074.
25. Hornak V, Abel R, Okur A, Strockbine B, Roitberg A, Simmerling C. Comparison of multiple Amber force fields and development of improved protein backbone parameters. *Proteins* 2006;65:712–725.
26. Case DA, Darden TA, Cheatham TE, III, Simmerling CL, Wang J, Duke RE, Luo R, Crowley M, Walker RC, Zhang W, Merz KM, Wang B, Hayik S, Roitberg A, Seabra G, Kolossaváry I, Wong KF, Paesani F, Vanicek J, Wu X, Brozell SR, Steinbrecher T, Gohlke H, Yang L, Tan C, Mongan J, Hornak V, Cui G, Mathews DH, Sasin MG, Sagui C, Babin V, Kollman PA. AMBER 10. San Francisco: University of California; 2008.
27. Bowers KJ, Chow E, Xu H, Dror RO, Eastwood MP, Gregersen BA, Klepeis JL, Kolossaváry I, Moraes MA, Sacerdoti FD, Salmon JK, Shan Y, Shaw DE. Scalable Algorithms for Molecular Dynamics Simulations on Commodity Clusters. *Proceedings of the ACM/IEEE Conference on Supercomputing (SC06)*, 2006.
28. Humphrey W, Dalke A, Schulter K. VMD: visual molecular dynamics. *J Mol Graph* 1996;14:33–38, 27–28.
29. Daura X, van Gunsteren WF, Mark AE. Folding-unfolding thermodynamics of a beta-heptapeptide from equilibrium simulations. *Proteins* 1999;34:269–80.
30. Gilson MK, Given JA, Bush BL, McCammon JA. The statistical-thermodynamic basis for computation of binding affinities: a critical review. *Biophys J* 1997;72: 1047–1069.
31. Hamelberg D, McCammon JA. Standard free energy of releasing a localized water molecule from the binding pockets of proteins: double-decoupling method. *J Am Chem Soc* 2004;126:7683–7689.
32. Beutler TC, Mark AE, van Shaik RC, Gerber PR, van Gunsteren WF. Avoiding singularities and numerical instabilities in free energy calculations based on molecular simulations. *Chem Phys Lett* 1994;529–539.
33. Chodera JD, Swope WC, Pitera JW, Seok C, Dill KA. *J Chem Theory Comput* 2007;3:26–41.
34. Zagrovic B, van Gunsteren W. Computational Analysis of the Mechanism and Thermodynamics of Inhibition of Phosphodiesterase 5A by Synthetic Ligands. *J Chem Theory Comput* 2007;3:301–311. doi: 10.1021/ct600322d.
35. Fujitani H, Tanida Y, Ito M, Jayachandran G, Snow CD, Shirts MR, Sorin EJ, Pande VS. Direct calculation of the binding free energies of FKBP ligands. *J Chem Phys* 2005;123:084108.
36. Shirts MR, Chodera JD. Statistically optimal analysis of samples from multiple equilibrium states. *J Chem Phys* 2008;129:124105.
37. Rueda M, Ferrer-Costa C, Meyer T, Pérez A, Camps J, Hospital A, Gelpí JL, Orozco M. A consensus view of protein dynamics. *Proc Natl Acad Sci USA* 2007;104:796–801.
38. Caves LS, Evanseck JD, Karplus M. Locally accessible conformations of proteins: multiple molecular dynamics simulations of crambin. *Protein Sci* 1998;7:649–666.
39. Monticelli L, Sorin EJ, Tielemans DP, Pande VS, Colombo G. Molecular simulation of multistate peptide dynamics: a comparison

- between microsecond timescale sampling and multiple shorter trajectories. *J Comput Chem* 2008;29:1740–1752.
40. Stoll V, Stewart KD, Maring CJ, Muchmore S, Giranda V, Gu YY, Wang G, Chen Y, Sun M, Zhao C, Kennedy AL, Madigan DL, Xu Y, Saldivar A, Kati W, Laver G, Sowin T, Sham HL, Greer J, Kempf D. Influenza neuraminidase inhibitors: structure-based design of a novel inhibitor series. *Biochemistry* 2003;42:718–727.
 41. Kati WM, Montgomery D, Carrick R, Gubareva L, Maring C, McDaniel K, Steffy K, Molla A, Hayden F, Kempf D, Kohlbrenner W. In vitro characterization of A-315675, a highly potent inhibitor of A and B strain influenza virus neuraminidases and influenza virus replication. *Antimicrob Agents Chemother* 2002;46:1014–1021.
 42. Abed Y, Nehme B, Baz M, Boivin G. Activity of the neuraminidase inhibitor A-315675 against oseltamivir-resistant influenza neuraminidases of N1 and N2 subtypes. *Antiviral Res* 2008;77:163–166.
 43. Baz M, Abed Y, Boivin G. Characterization of drug-resistant recombinant influenza A/H1N1 viruses selected in vitro with peramivir and zanamivir. *Antiviral Res* 2007;74:159–162.
 44. Bantia S, Parker CD, Ananth SL, Horn LL, Andries K, Chand P, Kotian PL, Dehghani A, El-Kattan Y, Lin T, Hutchison TL, Montgomery JA, Kellogg DL, Babu YS. Comparison of the anti-influenza virus activity of RWJ-270201 with those of oseltamivir and zanamivir. *Antimicrob Agents Chemother* 2001;45:1162–1167.
 45. Boivin G, Goyette N. Susceptibility of recent Canadian influenza A and B virus isolates to different neuraminidase inhibitors. *Antiviral Res* 2002;54:143–147.
 46. Gubareva LV, Webster RG, Hayden FG. Comparison of the activities of zanamivir, oseltamivir, and RWJ-270201 against clinical isolates of influenza virus and neuraminidase inhibitor-resistant variants. *Antimicrob Agents Chemother* 2001;45:3403–3408.
 47. Govorkova EA, Leneva IA, Goloubeva OG, Bush K, Webster RG. Comparison of efficacies of RWJ-270201, zanamivir, and oseltamivir against H5N1, H9N2, and other avian influenza viruses. *Antimicrob Agents Chemother* 2001;45:2723–2732.
 48. Hurt A, Selleck P, Komadina N, Shaw R, Brown L, Barr I. Susceptibility of highly pathogenic A(H5N1) avian influenza viruses to the neuraminidase inhibitors and adamantanes. *Antiviral Res* 2007;73:228–231.
 49. McSharry JJ, McDonough AC, Olson BA, Drusano GL. Phenotypic drug susceptibility assay for influenza virus neuraminidase inhibitors. *Clin Diagn Lab Immunol* 2004;11:21–28.
 50. Mishin VP, Hayden FG, Gubareva LV. Susceptibilities of antiviral-resistant influenza viruses to novel neuraminidase inhibitors. *Antimicrob Agents Chemother* 2005;49:4515–4520.
 51. Le QM, Kiso M, Someya K, Sakai YT, Nguyen TH, Nguyen KHL, Pham ND, Ngyen HH, Yamada S, Muramoto Y, Horimoto T, Takada A, Goto H, Suzuki T, Suzuki Y, Kawaoka Y. Avian flu: isolation of drug-resistant H5N1 virus. *Nature* 2005;437:1108.
 52. Shie J-J, Fang J-M, Wang S-Y, Tsai K-C, Cheng Y-SE, Yang A-S, Hsiao S-C, Su C-Y, Wong C-H. Synthesis of tamiflu and its phosphonate congeners possessing potent anti-influenza activity. *J Am Chem Soc* 2007;129:11892–11893.
 53. Yamashita M, Tomozawa T, Kakuta M, Tokumitsu A, Nasu H, Kubo S. CS-8958, a prodrug of the new neuraminidase inhibitor R-125489, shows long-acting anti-influenza virus activity. *Antimicrob Agents Chemother* 2009;53:186–192.